Solid state core-exciton dynamics in NaCl observed by tabletop attosecond four-wave mixing spectroscopy

James D. Gaynor[1,2,*] Ashley P. Fidler[1,2,†] Yen-Cheng Lin[1,2] Hung-Tzu Chang[1] Michael Zuerch[1,3] Daniel M. Neumark[1,2,‡] and Stephen R. Leone[1,2,4,§]

[1]*Department of Chemistry, University of California, Berkeley, California 94720, USA*
[2]*Chemical Sciences Division, Lawrence Berkeley National Laboratory, Berkeley, California 94720, USA*
[3]*Materials Science Division, Lawrence Berkeley National Laboratory, Berkeley, California 94720, USA*
[4]*Department of Physics, University of California, Berkeley, California 94720, USA*

(Received 5 March 2021; accepted 8 June 2021; published 25 June 2021)

Nonlinear wave mixing in solids with ultrafast x-rays can provide insight into complex electronic dynamics of materials. Here, tabletop-based attosecond noncollinear four-wave mixing (FWM) spectroscopy using one extreme ultraviolet (XUV) pulse from high harmonic generation and two separately timed few-cycle near-infrared (NIR) pulses characterizes the dynamics of the Na^+ $L_{2,3}$ edge core-excitons in NaCl around 33.5 eV. An inhomogeneous distribution of core-excitons underlying the well-known doublet absorption of the Na^+ Γ point core-exciton spectrum is deconvoluted by the resonance-enhanced nonlinear wave mixing spectroscopy. In addition, other dark excitonic states that are coupled to the XUV-allowed levels by the NIR pulses are characterized spectrally and temporally. Approximately < 10 fs coherence lifetimes of the core-exciton states are observed. The core-excitonic properties are discussed in the context of strong electron-hole exchange interactions, electron-electron correlation, and electron-phonon broadening. This investigation successfully indicates that tabletop attosecond FWM spectroscopies represent a viable technique for time-resolved solid state measurements.

DOI: 10.1103/PhysRevB.103.245140

I. INTRODUCTION

The explosive development of ultrafast nonlinear spectroscopy with extreme ultraviolet (XUV) and x-ray light pulses from both tabletop high harmonic generation (HHG) and x-ray free-electron lasers (XFELs) is rapidly advancing our knowledge of atoms, molecules, and materials [1]. XFELs now produce <100 fs light pulses at subnanometer wavelengths with intensities up to 10^{20} W cm^{-2} [2]. The high pulse intensities lend well to exploring many long-predicted nonlinear pulse sequences of multiple XUV/x-ray fields [3], such as x-ray stimulated Raman based methods [4], multidimensional x-ray experiments [5], soft x-ray second harmonic generation [6], and four-wave mixing (FWM) spectroscopy with x rays [7]. Sources using HHG produce XUV and soft x-ray pulses of broad coherent spectral bandwidth that support attosecond temporal resolution—characteristics that are ideal for capturing electronic dynamics that typically occur at <10 fs timescales [1,2]. The flexibility and autonomy of tabletop XUV sources in a modern optics laboratory allow complicated nonlinear experiments and pulse sequences to be developed and quickly refined, such as those requiring multiple optical and near-infrared (NIR) pulses in noncollinear beam geometries [8,9].

Using XFELs, condensed matter physicists have exploited the high-flux, <50 nm XUV wavelength pulses in transient-grating experiments with two time-coincident XUV pulses to form a spatially periodic excitation profile followed by a third pulse to measure electric susceptibilities and phonon propagation on length scales of several nanometers [10–13]. Using HHG sources, attosecond noncollinear FWM spectroscopy has measured electronic, vibrational, and vibronic dynamics in gas-phase atoms and molecules, characterizing excited state valence and Rydberg wave packets and the influence of nearby dark states with subfemtosecond temporal resolution and elemental selectivity [8,9,14,15]. The attosecond FWM experiment utilizes signal enhancement through three resonant transitions between core-level states and neighboring states, background free detection of the XUV signal due to a noncollinear beam geometry, subfemtosecond synchronization with an array of optical pulses that can be combined with the XUV, and subfemtosecond time-domain tracking of core-excited state evolution through double-quantum coherence [16] transition pathways. The success of attosecond FWM experiments in atomic and molecular physics suggests that this methodology can advance investigations of atomlike core-excitonic phenomena in solid state materials as well. We connect the atomic and the solid state physics communities in this paper by implementing tabletop attosecond FWM spectroscopy to successfully measure core-level excited state phenomena of the solid state insulator NaCl at the Na^+ $L_{2,3}$ edge near 33.5 eV.

*Corresponding author: jgaynor@berkeley.edu
†Present address: Department of Chemistry, Princeton University, Princeton, New Jersey 08544, USA.
‡dneumark@berkeley.edu
§srl@berkeley.edu

Alkali halides are insulators with important electrical and optical properties arising from a large energy gap between their valence and conduction bands [17]. They are the simplest ionic solids, consisting of equal numbers of monovalent cation-anion species. Decades of investigations on the short-range interactions of bound electron-core-hole pairs in these materials (core-level excitons or "core-excitons") have aimed to characterize the nature of core-exciton states formed in alkali halides, such as NaCl [18–30], where some are associated with Na^+ and some with Cl^-. Weak dielectric screening inherent to wide gap insulators enhances electron-hole attraction; the highly localized electronic structure of the core-exciton approaches that of a Frenkel exciton [17,18,27,31]. In this highly localized limit, similarities to the electronic properties of atomic orbitals can aid the understanding of core-excitonic phenomena [32,33]. The elemental specificity of XUV and x-ray spectroscopy is ideal for probing these very localized electronic dynamics that reflect complex interactions between electrons and nuclei. Moreover, nonlinear spectroscopies using XUV pulses have the potential to unravel information, such as inhomogeneous broadening, that is typically hidden in linear absorption-based methods [7,34] while exploiting this elemental specificity.

The class of third-order nonlinear techniques, which includes XFEL-based transient-grating experiments and attosecond FWM spectroscopy, specifies each of three incident fields by unique wave vectors to account for the emitted signals as the fourth wave. Attosecond FWM spectroscopy temporally resolves the system evolution between all three pulses and resonantly drives double-quantum coherence pathways used to generate the signal. The high temporal resolution achieved in the tabletop attosecond FWM spectroscopies is crucial for measuring dynamics on <10 fs timescales. Here, attosecond FWM spectroscopy is applied to characterize the highly localized Na^+ core-exciton measured at the Na^+ $L_{2,3}$ absorption edge on the <10 fs timescale. We find that several more Na^+ core-excitons underlie the Na^+ $L_{2,3}$ absorption than previously reported and that there are very different temporal dynamics that can be observed on such timescales. Distinct spectral and temporal behaviors of the time-resolved XUV emission are measured for both XUV bright states and a subset of XUV dark states that are uniquely probed with this method. The nonlinear nature and phase-matching dependence of the attosecond FWM experiment enables us to show that the well-known NaCl core-exciton absorption arises from a heterogeneous distribution of at least five core-exciton states.

II. RESULTS

A. The XUV spectrum of NaCl

The linear absorption spectrum of a 50-nm-thick NaCl microcrystalline film from 32.5 to 37.5 eV is shown in Fig. 1 (see Appendix B for NaCl thin film sample details). The strong absorption features in the 33.2–33.8 eV region arise from the absorption to core-excitonic states—bound electron-hole pairs involving a core-hole—at the Na^+ $L_{2,3}$ edge. From the atomic perspective, this is the excitation of a $2p$ electron resulting in the Na^+ $2s^2 2p^5 3s$ electronic configuration [18,19,31]. From

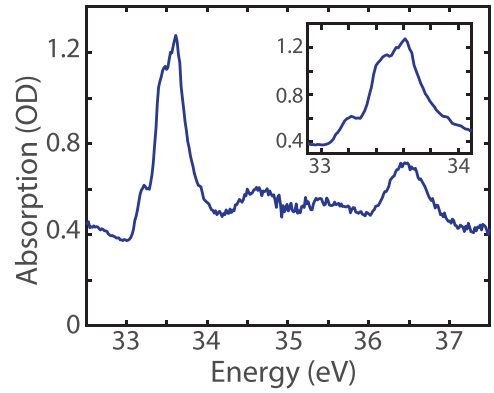

FIG. 1. Linear extreme ultraviolet (XUV) absorption spectrum of NaCl around Na^+ $L_{2,3}$ edge. The linear absorption spectrum of a NaCl thin film (50 nm) used in the four-wave mixing (FWM) experiments of the Na^+ $L_{2,3}$ edge. The inset zooms in on the Na^+ core-exciton absorption features of interest in this paper.

a band structure perspective, the resemblance between the Na^+ $L_{2,3}$ edge spectrum and the UV absorption spectrum has resulted in the XUV features being ascribed to core-excitons at the Γ point in the Brillouin zone [18]. Three peaks comprise the lowest energy absorption band in Fig. 1 (inset), one weaker feature at 33.27 eV and two stronger overlapping peaks at 33.42 and 33.61 eV. In previous literature, the predominant doublet structure between one strong higher energy feature and one weaker lower energy feature is widely attributed to spin-orbit splitting, as is observed in the fundamental UV absorption spectrum [18]. To our knowledge, the partial splitting of the strong higher energy feature is not reported in the XUV absorption literature, but such splittings have been observed for valence excitons in the UV range and are considered further in terms of lattice imperfections and surface states in the Discussion section. Photoelectron measurements of the Na^+ $2p$ core-exciton have shown XUV spectra with greater width than expected and a similar shoulder peak structure to the absorption spectrum in Fig. 1 (inset), which are suggested, but not confirmed, to be due to surface states [35]. Due to the p-orbital symmetry of the core-hole, a triply degenerate state is expected in the absence of any energetic splitting. The specific origin of the weak band spanning 34–36 eV is not widely agreed upon, but it has been ascribed to transitions into bound electron-hole states lying just below the onset of the conduction band [19,20]. The peak centered at 36.5 eV corresponds to excitonic formation at a different point in the Brillouin zone [19,21], which is energetically like the Na^+ free ion $2s^2 2p^5 3p$ configuration [31]. The $\sim$0.4 optical density (OD) continuous absorption background is due to valence band transitions into high-lying conduction band states [18,19].

B. Attosecond XUV-NIR FWM spectroscopy of NaCl core-excitons

The schematic in Fig. 2(a) illustrates the principle of the attosecond FWM experiment. An attosecond pulse train ($\mathbf{k}_{XUV}$) consisting of 2–3 subfemtosecond bursts in the XUV spanning 25–45 eV is focused through the aperture of a silver-coated annular mirror onto the NaCl microcrystalline thin film

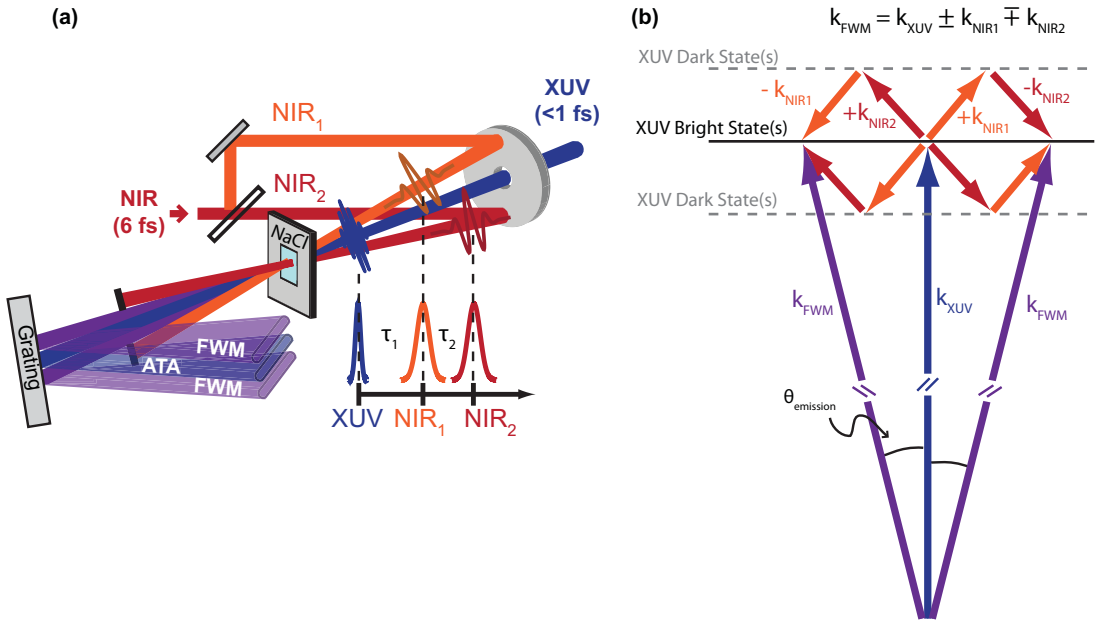

FIG. 2. Attosecond extreme ultraviolet (XUV) near-infrared (NIR) four-wave mixing (FWM) spectroscopy in a noncollinear beam geometry. (a) Schematic of the beam geometry and pulse sequence. Two few-cycle NIR beams (k_{NIR1}/NIR_1, orange; k_{NIR2}/NIR_2, red) are vertically stacked and crossed with an attosecond XUV pulse train (k_{XUV}/XUV, blue) on the NaCl sample. The delays between each beam are independently tunable; the XUV-NIR delay is denoted τ_1, and the delay between the two NIR pulses is τ_2. The wave mixing signals (k_{FWM}) are emitted at an angle $\theta_{emission}$, and the attosecond transient absorption (ATA) signals are collinear with the XUV pulse. (b) The initially excited XUV-bright states are coupled through XUV-dark states and back to the bright state manifold through the two sequential NIR interactions. The phase-matching condition determines the emitted signal direction. Controlling the pulse timing determines whether the time-resolved XUV emission arises from the evolution of the XUV-bright states or the XUV-dark states.

sample. Two independently controlled NIR beams ($\mathbf{k}_{NIR1}$, $\mathbf{k}_{NIR2}$), spanning 550–950 nm (1.3–2.25 eV), are each routed through translational delay stages and then spatially overlapped with the XUV beam on the NaCl sample by reflection with the annular mirror. The delay stages controlling the XUV-NIR time delay (τ_1) and the NIR_1-NIR_2 time delay (τ_2) are arranged in series to optimize timing precision and stability in the time-dependent experiments discussed below.

As shown in Fig. 2(b), the broadband XUV pulse excites the core-excitons at the Na^+ $L_{2,3}$ edge. One NIR interaction induces transitions from the core-excitonic excited states to a nearby XUV-dark state manifold; the second NIR interaction transfers the excited system back to an XUV-allowed manifold of core-excited states. The detected signals arise from the XUV emission of these excited states back to the ground state. After the sample, an Al foil (0.15 μm thick) filters out the NIR beams and transmits the generated XUV signals, which are spectrally dispersed and imaged onto an x-ray charge-coupled device (CCD) camera. A more complete experimental description is published elsewhere [8,9], and details are in Appendix A.

Each of the ith fields in the attosecond FWM experiment can be expressed as $\mathbf{E}_i(t) = A_i(t - t_i)\exp\{-i[\omega_i(t - t_i) + \phi_i]\}\exp(-i\mathbf{k}_i \cdot \mathbf{r})$ with a temporal profile $A_i(t - t_i)$ centered at t_i, a carrier frequency ω_i, phase ϕ_i, and a unique wave vector $\mathbf{k}_i$ directionally projected onto a laboratory frame coordinate vector $\mathbf{r}$. The noncollinear beam geometry exploits the phase-matching condition

$$\mathbf{k}_{FWM} = \mathbf{k}_{XUV} \pm \mathbf{k}_{NIR1} \mp \mathbf{k}_{NIR2}, \tag{1}$$

during the sequential light-matter interactions via the third-order susceptibility $\chi^{(3)}$ of the sample [34]. The momentum conservation requirement of Eq. (1) results in the emission of spatially distinct XUV wave mixing signals that can be detected background free [8,9,14,15]. The FWM emission angle $\theta_{emission}$ is easily calculated from the photon energies of the incident pulses (ω_{XUV}, ω_{NIR1}, ω_{NIR2}) and the crossing angles between the NIR beams and the XUV beam according to the following relation:

$$\theta_{emission} = \frac{\omega_{NIR1}\theta_1 + \omega_{NIR2}\theta_2}{\omega_{XUV}}, \tag{2}$$

where θ_1 (θ_2) is the angle between $\mathbf{k}_{XUV}$ and $\mathbf{k}_{NIR1}$ ($\mathbf{k}_{NIR2}$). The chosen beam geometry results in vertically displaced wave mixing signals with respect to the XUV pulse such that $\mathbf{k}_{XUV}$ is centered on the x-ray CCD camera at $\theta_{emission} \approx 0$ mrad, and the grating spectrally disperses in the horizontal dimension. As implied in Fig. 2(a), the attosecond transient absorption (ATA) signal is also generated from two interactions with the same NIR pulse (e.g., $\mathbf{k}_{ATA} = \mathbf{k}_{XUV} + \mathbf{k}_{NIR1} - \mathbf{k}_{NIR1}$), emitted collinearly with $\mathbf{k}_{XUV}$, which can be simultaneously measured with the FWM signals.

At temporal overlap of all three incident pulses ($\tau_1 = 0$, $\tau_2 = 0$), many different transition pathways are possible. The FWM pathways relevant to this discussion are illustrated in Fig. 2(b), all of which require initial excitation by $\mathbf{k}_{XUV}$. In principle, transition pathways including XUV-dark states that are within the NIR bandwidth are allowed; they may be either higher or lower in energy than the initially excited XUV-bright states. The double-quantum coherence transition

pathways giving rise to the FWM signal observed at a given emission angle from different dark states ensure the signals do not cancel.

The decay dynamics of the XUV-excited states can be measured by keeping NIR_1 and NIR_2 temporally overlapped with each other ($\tau_2 = 0$) and scanning the XUV-NIR delay (τ_1); we refer to this as a "bright state scan." In a bright state scan, the phase-matching condition permits FWM signals with equivalent information content to be emitted at positive angles ($+\theta_{\text{emission}}$; located spatially above $\mathbf{k}_{\text{XUV}}$) and negative angles ($-\theta_{\text{emission}}$; located spatially below $\mathbf{k}_{\text{XUV}}$). Additionally, the effect of the coherently excited dark states on the XUV emission can be measured by setting $\tau_1 = 0$ while τ_2 is scanned; we refer to this as a "dark state scan." The dark state scan effectively drives a two-photon excitation (XUV ± NIR) into any XUV-dark state that has an appreciable transition dipole moment connecting the bright and dark state manifolds. The evolution of these dark states can then be monitored by scanning τ_2. Notably, the information symmetry between the FWM signals measured at $\pm\theta_{\text{emission}}$ is broken in the dark state scan as soon as τ_2 is beyond pulse overlap due to the phase-matching condition. Provided there are dark states accessible at lower and higher energies relative to the XUV-bright states, the selective measurement of the dynamics within two different dark state manifolds is possible by targeting the collection of FWM signal at either positive or negative θ_{emission}. As shown below for the NaCl core-excitons at the Na^+ $L_{2,3}$ edge, the dark state scans can also help to narrow down the set of states participating in the bright state transition pathways.

The Na^+ core-exciton states observed in the XUV spectrum (Fig. 1) are measured using attosecond FWM spectroscopy and shown in Fig. 3(a) at temporal overlap of all three pulses ($\tau_1 = 0$, $\tau_2 = 0$). The FWM emission is centered at $\theta_{\text{emission}} \approx \pm 2.2$ mrad, in agreement with the expected divergence angles of $\theta_{\text{emission}} \approx \pm 1.4$–$2.4$ mrad for NIR crossing angles (θ_1, θ_2) of 18 mrad; the beam geometries are illustrated above the spectra. The differential absorption is plotted as $\Delta A = -\log(I/I_0)$, where I is the signal collected with all beams incident on the sample and I_0 is the signal collected when both NIR beams are blocked by an automated shutter. The I_0 spectrum comprises dark counts from the CCD and residual scattered light from the XUV and collinear NIR beams used for HHG [8]. As mentioned above, the ATA signals can be collected simultaneously with the FWM signals due to the different angular dependences of the emissions. The ATA phase matching conditions result in emitted signals collinear with $\mathbf{k}_{\text{XUV}}$ at θ_{emission} centered around 0 mrad. The angular dispersion of the ATA signal in the $-1 < \theta_{\text{emission}} < 1$ mrad range is dependent upon the generation and focusing conditions of $\mathbf{k}_{\text{XUV}}$. The FWM signals are homodyne detected, whereas the ATA signals utilize the collinear $\mathbf{k}_{\text{XUV}}$ as an intrinsic local oscillator for self-heterodyned detection [8]. Thus, only the signal fields interfering with $\mathbf{k}_{\text{XUV}}$ contribute nonnegligible intensity to the ATA signal; intensity resulting from the individual ATA signal fields adding in quadrature with each other is negligible. As a result of the self-heterodyned detection, bleach/emission (negative) and induced absorption (positive) features are distinguished in the ATA differential absorption, and the intensity of the ATA signal is expected to be two times as strong, rather than four times, with both NIR beams present.

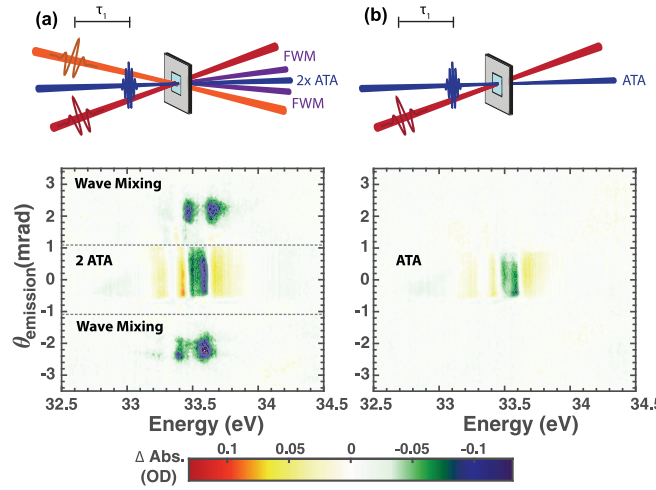

FIG. 3. Extreme ultraviolet (XUV) near-infrared (NIR) nonlinear wave mixing signal of Na^+ core-excitons in NaCl. (a) The Na^+ $L_{2,3}$ core-exciton signal observed under the four-wave mixing (FWM) experimental conditions (all beams unblocked, pulse sequence above) at temporal overlap ($\tau_1 = \tau_2 = 0$). The background-free FWM signals are observed at $|\theta_{\text{emission}}| > 1$ mrad, while the attosecond transient absorption (ATA) signals are found in the range $-1 < \theta_{\text{emission}} < 1$ mrad; $-\Delta$OD indicates optical density of emission. (b) Confirmation of the nonlinear wave mixing nature of the detected signals from blocking $\mathbf{k}_{\text{NIR1}}$; only the ATA signal from $\mathbf{k}_{\text{NIR2}}$ is observed as expected. To avoid detector saturation, the ATA signals are collected with 0.7 s integration, while the FWM signals are collected with 2.0 s integration, resulting in the FWM signals shown in (a) effectively enhanced relative to the ATA signals by ∼2.86.

Each of the two noncollinear NIR beams required for the FWM experiment generates ATA signal. Thus, the ATA signal measured in Fig. 3(a) is the sum of two equivalent ATA signals—one from each NIR beam. To confirm that the observed signals above and below the ATA region result from the FWM nonlinear process involving $\mathbf{k}_{\text{XUV}}$, $\mathbf{k}_{\text{NIR1}}$, and $\mathbf{k}_{\text{NIR2}}$, a spectrum was collected with $\mathbf{k}_{\text{NIR1}}$ blocked and is shown in Fig. 3(b). As expected, the FWM signals observed at $|\theta_{\text{emission}}| > 1$ mrad vanish, and the ATA signal measured at $-1 < \theta_{\text{emission}} < 1$ mrad is approximately half of the intensity of that measured in Fig. 3(a). We note that the ATA signals often require lower CCD exposure times to avoid pixel saturation from $\mathbf{k}_{\text{XUV}}$ affecting the differential absorption measurement. Thus, the ATA signals were collected with 0.7 s CCD exposure, and the FWM signals were collected with 2.0 s exposure resulting in the FWM signals effectively enhanced relative to the ATA signals by a corresponding factor of $\frac{2.0}{0.7} \cong 2.86$.

The magnitude of the strongest FWM signal from the core-exciton at 33.61 eV is plotted as a function of NIR fluence in Fig. 4(a). The linear dependence on energy fluence with each NIR pulse gives additional confirmation of the FWM nature of the reported signals [12]. Higher-order signals (e.g., six-wave mixing) are expected to be negligible as signal magnitudes decrease for each successively higher electric field dependence [34]. The three most intense core-exciton features at temporal

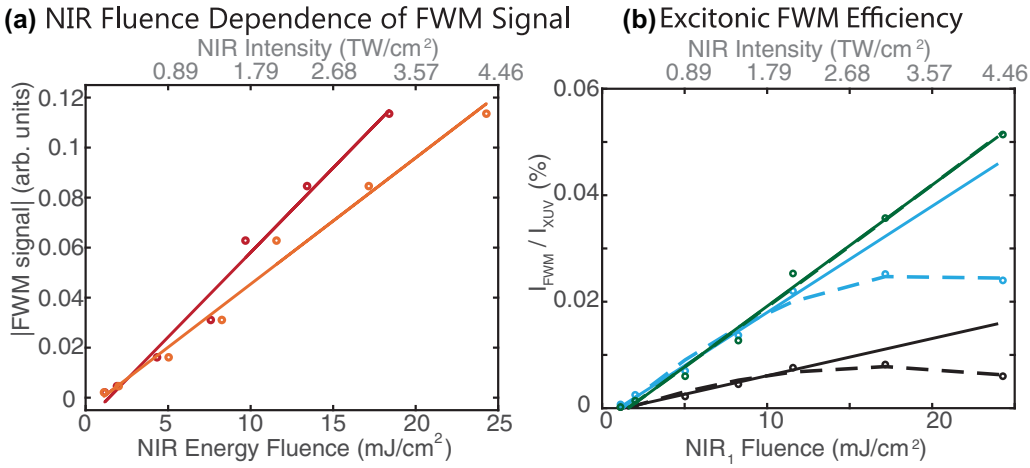

FIG. 4. Near-infrared (NIR) fluence dependence and generation efficiency of the four-wave mixing (FWM) signal. (a) The NIR fluence dependence of the strongest Na^+ core-exciton at 33.61 eV for $\mathbf{k}_{NIR1}$ (orange) and $\mathbf{k}_{NIR2}$ (red); spectra are collected at temporal overlap. (b) The excitonic FWM efficiency calculated for the three main core-excitons with increasing $\mathbf{k}_{NIR1}$ fluence observed at temporal overlap. Linear (solid) and quadratic (dashed) fits; 33.27 eV = black, 33.42 eV = light blue, and 33.61 eV = green. Fluence dependence of FWM signal and excitonic efficiencies are all linear $<12\,mJ/cm^2$ ($<2.14\,TW/cm^2$), NIR fluences in the 8–10 mJ/cm^2 (1.43–1.79 TW/cm^2) were used in the FWM studies to stay in the linear regime.

overlap are measured to have different FWM signal generation efficiencies, defined as the ratio of the integrated intensities of the FWM signal magnitude (I_{FWM}) and the incident XUV pulse (I_{XUV}), I_{FWM}/I_{XUV}. Figure 4(b) presents the FWM efficiency for the excitons at 33.27 eV (black), 33.42 eV (light blue), and 33.61 eV (green) as a function of NIR_1 fluence. A linear increase for all three core-excitons up to 12 mJ/cm^2 (2.14 TW/cm^2) of NIR fluence is evident, and the data for each core-exciton are best fit to a straight line up through this value (solid lines). However, the core-excitons at 33.26 and 33.42 eV behave nonlinearly with plateaus in the FWM efficiencies for NIR_1 fluences $>12\,mJ/cm^2$ ($>2.14\,TW/cm^2$), as shown by the quadratic polynomial fits (dashed lines). There is a negligible difference between the linear and quadratic fits for the 33.61 eV core-exciton through NIR fluences of 25 mJ/cm^2 (4.46 TW/cm^2). A possible explanation for the varied FWM efficiencies with increasing NIR fluence is that the three core-exciton states utilize different dark states in the wave mixing process. For example, the two core-excitons with saturating efficiencies at high NIR fluences could involve dark states that are more susceptible to multiphoton absorption effects. Aside from the fluence dependence measurement, all experiments reported here were performed with NIR pulse fluences of 8–10 mJ/cm^2 (1.43–1.79 TW/cm^2) to minimize undesirable multiphoton effects.

C. Core-exciton dynamics resonantly probed with FWM spectroscopy

In the bright state scan configuration, the transient FWM signals track the temporal evolution of the core-excitonic wave packet that is excited by $\mathbf{k}_{XUV}$. The time-dependence of the Na^+ core-exciton states is measured in the bright state scan shown in Fig. 5(a). The transient spectrum is obtained by plotting the integrated FWM signal ($-2 \geqslant \theta_{emission} \geqslant -2.4$ mrad) as τ_1 is scanned. While the same information is present in the FWM signal at $+\theta_{emission}$ in the bright state scan, the signal at negative emission angles was easier to isolate experimentally from the ATA signal and the residual XUV scattered light by using a combination of irising and filtering upstream in the HHG beamline (see Appendix A). Coherence decay times of 7.1 ± 0.9 and 6.7 ± 0.8 fs were determined for the bright state scan line outs at 33.42 and 33.61 eV, respectively, by fitting the traces to a single exponential decay convolved with Gaussian instrument response functions of 5.2 ± 0.9 and 5.1 ± 0.8 fs. The lowest energy feature centered at 33.27 eV during temporal overlap is weaker in magnitude and appears to have comparable lifetimes with the higher energy peaks but undergoes an ∼0.08 eV blueshift over the initial 20 fs of core-exciton relaxation.

In the dark state scan configuration, the initial two-photon interaction ($\mathbf{k}_{XUV} \pm \mathbf{k}_{NIR1}$) excites a wave packet propagating in XUV-forbidden states that are within the few-cycle NIR bandwidth ($\omega_{XUV} \pm \omega_{NIR1}$). The dark state wave packet is monitored by plotting the same integrated range of $\theta_{emission}$ as in the bright state scan for each τ_2 delay of $\mathbf{k}_{NIR2}$. Figure 5(b) shows the transient FWM dark state signal corresponding to the phase-matched transition pathways with $\mathbf{k}_{FWM} = \mathbf{k}_{XUV} + \mathbf{k}_{NIR1} - \mathbf{k}_{NIR2}$ momentum conservation after pulse overlap; this is a consequence of the geometric orientation of the pulses and the temporal causality enforced by the relative pulse timings. That is, since $\mathbf{k}_{NIR1}$ is aligned spatially above $\mathbf{k}_{XUV}$ before the sample, the phase-matched FWM signals from the $\mathbf{k}_{XUV} + \mathbf{k}_{NIR1}$ interaction will appear at $-\theta_{emission}$, which is the signal of interest here. The dark states involved most strongly with all the measured FWM signals can thus be determined to be greater in energy than the XUV-excited Na^+ core-excitons due to the minimal time-dependent FWM signal of dark state scans at $+\theta_{emission}$ (see Supplemental Material, Fig. SM1 [36]).

The spectral profile of the dark state scan significantly differs from the bright state scan in Fig. 5. While the core-excitons measured at $\tau_2 = 0$ have the same peak positions as the bright state scan (33.27, 33.42, and 33.61 eV), the peak

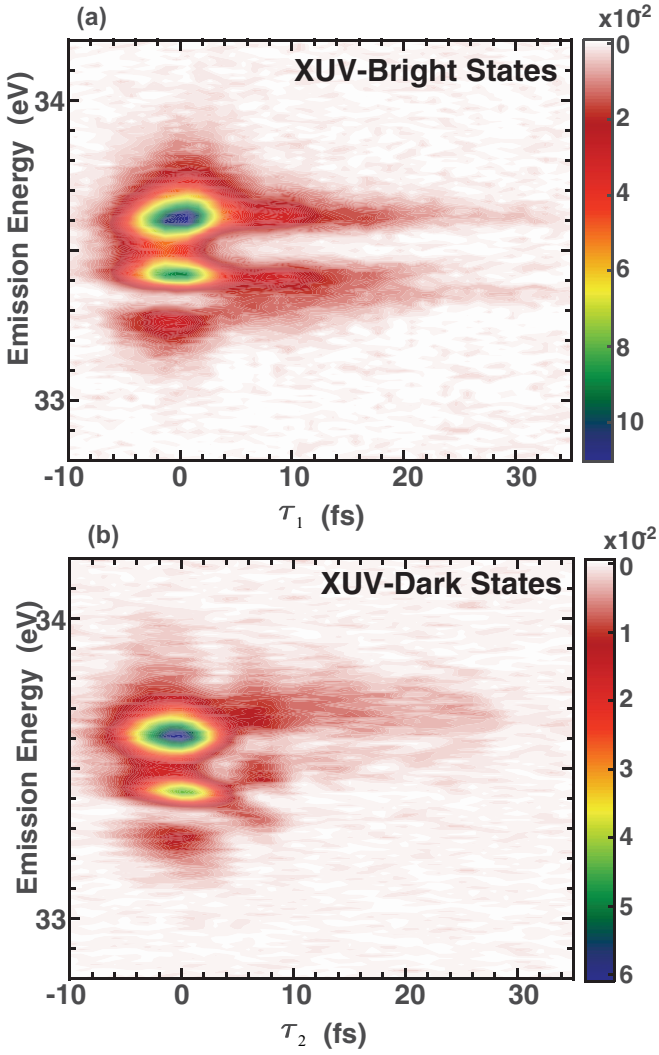

FIG. 5. Time-dependent four-wave mixing (FWM) signals measure excitonic dynamics. (a) Time-resolved extreme ultraviolet (XUV) emission of the FWM signal ($-2.0 > \theta_{\text{emission}} > -2.4$ mrad) collected as a function of XUV-bright state evolution (τ_1 scanned, $\tau_2 = 0$). (b) Time-resolved XUV emission of FWM signal collected as a function of XUV-dark state evolution following initial two photon ($\mathbf{k}_{\text{XUV}} + \mathbf{k}_{\text{NIR1}}$) excitation into the XUV-dark states ($\tau_1 = 0$, τ_2 scanned).

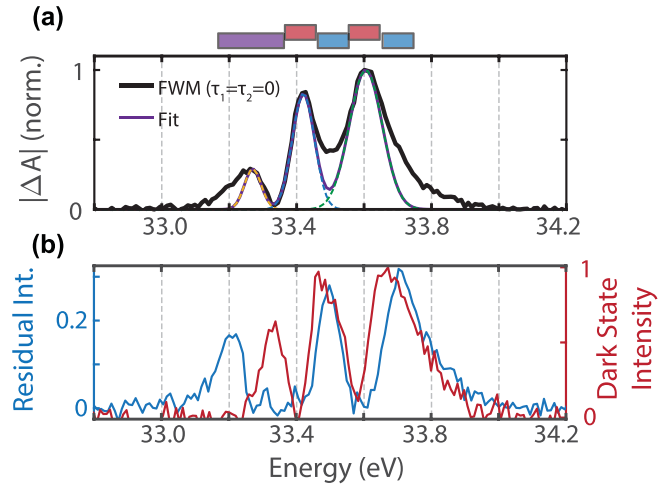

FIG. 6. Deconvolution of core-exciton four-wave mixing (FWM) signals. Spectral deconvolution of the time-zero spectrum with core-excitonic components identified in both the bright and dark state scans. (a) Temporal overlap FWM spectrum (black) fit with the three primary core-excitons identified in the bright state scans with Gaussian distributions and (b) the fit residuals (blue, left axis) compared with the core-excitons (normalized, red, right axis) identified in the dark state scans following overlap at a 7 fs delay. The blocks above the top plot highlight the five distinct core-excitonic regions discussed in the text. The red blocks refer to distinct states observed only in the bright state scan in (a); blue blocks refer to distinct states identified through the comparison of the residuals and dark state scans in (b) and the purple block on the low energy region highlights features observed in both (a) and (b), which may correspond to more than one distinct state.

positions shift to 33.34, 33.47, and 33.67 eV by $\tau_2 = 7$ fs in the transient dark state scan. The decay of the 33.67 eV peak can be fit to a single exponential yielding an 8.1 ± 1.0 fs coherence decay. It is difficult to retrieve meaningful decay times from the lower energy peaks without invoking a more complex kinetic model because of the different spectral profile observed at 7 fs in comparison with that at temporal overlap.

A spectral fitting of the FWM signal at temporal overlap is shown in Fig. 6. A snapshot of the core-excitons accessible upon initial excitation is determined by fitting the FWM spectrum at temporal overlap to the states observed in the bright state scan [Fig. 6(a)] and then comparing the residuals to the core-excitons measured independently in the dark state scan at 7 fs [Fig. 6(b)]. The inhomogeneous broadening of the excitons is evident when Gaussian distributions are used to provide the best fit to the line shapes in Fig. 6(a). The peak fits in Fig. 6(a) are centered at the bright state excitonic energies 33.27, 33.42, and 33.61 eV, which have full width at half maximum (FWHM) linewidths of 0.050, 0.066, and 0.098 eV, respectively. The underlying background absorption has been subtracted, and the spectra are normalized to the 33.61 eV peak for fitting analysis. The peaks are fit with amplitudes of 0.29, 0.83, and 1.00, respectively. The core-excitonic spectrum from the dark state scan in Fig. 6(b) at $\tau_2 = 7$ fs is in very good agreement with the fit residuals for the two higher energy features centered at 33.47 and 33.67 eV, but less so for the lowest energy feature. The spectral resolution of these individual components demonstrated in Fig. 6 is a notable result demonstrating the power of these nonlinear experiments.

III. DISCUSSION

Previous interpretations of the core-excitonic spectra at the Na^+ $L_{2,3}$ edge in NaCl have relied heavily on the understanding of valence-excitonic spectra measured in the UV due to their close resemblance [18,19,22]. It is well known that the valence exciton in NaCl consists of the excitation of a Cl^- $3p$ electron to a neighboring Na^+ $3s$ orbital, which remains bound to the $3p$ hole on the Cl^- ion [22,23,30]. The electron is localized on the Na atom with s-orbital-like symmetry for both the valence exciton and the core-exciton [18,23,24]. The core-exciton at the Na^+ $L_{2,3}$ edge is expected to have a smaller excitonic radius than the valence exciton due to the hole also

being confined to the Na $2p$ orbital. The predominant doublet structure, reported widely in the linear absorption of both the valence exciton and the core-exciton, is typically ascribed to spin-orbit splitting of the p orbitals [18,19,22,25]. However, we observe more distinct core-excitonic components through the spectral deconvolution of the Na^+ $L_{2,3}$ absorption edge using attosecond nonlinear FWM spectroscopy than is observed in the linear spectrum of Fig. 1(inset).

A. Deconvolving inhomogeneous distributions of Na^+ core-excitonic states

The nonlinear wave mixing spectroscopy used here exploits the dependence of the FWM signal on three incident electric fields to isolate different core-excitonic subensembles within the inhomogeneous distribution of excitonic states present at the Na^+ $L_{2,3}$ edge. Importantly, this is achieved through resonantly driving the transitions between XUV-bright and XUV-dark states using the two noncollinear NIR pulses. Clear evidence that at least five distinct core-excitonic states underlie this absorption band is revealed by the transient FWM data in Fig. 5 and the spectral deconvolution in Fig. 6. It is well established from previous wave mixing studies of atomic and molecular gas phase systems that different wave mixing signals may contribute through Λ-type, V-type, and ladder-type transition pathways [8,9,15]. The combination of bright and dark state spectra with signal selectivity at positive and negative θ_{emission} in Figs. 5 and SM1 in the Supplemental Material [36] confirms that pathways analogous to the Λ-type atomic transitions are the primary contributors to the observed signals. Further, the lack of contributions from ladder-type transitions is confirmed by the absence of FWM signal measured in the range $1.4 \leqslant |\theta_{\text{emission}}| \leqslant 2.4$ mrad in Fig. 3(b); such signals would appear through two-photon transitions originating from higher- (or lower-) lying XUV-bright states driven by one NIR pulse with the phase-matching condition $\mathbf{k}_{\text{FWM}} = \mathbf{k}_{\text{XUV}} + \mathbf{k}_{\text{NIR1}} + \mathbf{k}_{\text{NIR1}}$ or $\mathbf{k}_{\text{FWM}} = \mathbf{k}_{\text{XUV}} - \mathbf{k}_{\text{NIR1}} - \mathbf{k}_{\text{NIR1}}$ (or similarly for $\mathbf{k}_{\text{NIR2}}$). The experiments demonstrate that the dark states must be energetically situated within the bandwidth of one NIR photon greater in energy (within 1.3–2.2 eV) of the XUV excited core-excitons. They must also have p-orbital-like symmetry to carry nonnegligible oscillator strength for the transition from the excited core-excitonic states with s-orbital symmetry localized on the Na^+ core.

The time dependence of the bright state FWM signals in Fig. 5(a) distinguishes the nature of the core-excitons at 33.42 and 33.61 eV from the core-exciton at 33.27 eV. The two higher energy core-excitons decay monoexponentially on the few-femtosecond timescale without any change in spectral position or shape. There is possibly some evidence of a weak recurrence around $\tau_1 = 8$ fs resembling a coherent oscillation in these two features as well. These decays reflect the dephasing timescales of core-excitonic states with relatively stable energies since no significant shift in line shape is measured during the decay. A different dynamic is observed in the lowest energy core-exciton, which blueshifts by ~0.08 eV over ~20 fs. While the origin of this dynamic is not yet certain, possible explanations include core-hole stabilization for a nonequilibrated core-exciton or excitonic wave function motion away from its initial excited state configuration on this timescale.

Recent attosecond studies of core-exciton dynamics in Si [32] and MgO [33] have alluded to the importance of dark excitons. Attosecond FWM spectroscopy has the unique ability to directly measure the effect of the dark states on the evolution of the initially excited ensemble of core-excitons. The spectral shifting observed in the NaCl dark state scans by 7 fs after temporal overlap [Fig. 5(b)] arises from the dark state excitonic wave packet propagating away from the electronic distribution of initially excited states—analogous to an excited state molecular wave packet moving away from the Franck-Condon region [9]. Following previous assignments of the Na^+ $L_{2,3}$ absorption to core-excitons at the Γ point in the Brillouin zone [18], the observed dynamics would reflect the excitonic system propagating away from the Γ point. However, without knowledge of the specific dark states involved in the measured pathways, it is unclear to what extent the band picture can be applied. We note the discrepancy between the single particle band picture and the highly localized excitonic picture here and emphasize that we cannot confirm the band picture from our measurements.

To better understand the dark state scan data, consider that the nonlinear wave mixing signal strengths are proportional to the product of the four transition dipole moments driven through the field-matter interaction $\mu_{\text{XUV}}\mu_{\text{NIR1}}\mu_{\text{NIR2}}\mu_{\text{FWM}}$, where the subscripted labels correspond to those of the electric field wave vectors in the experimental pulse sequence [Eq. (1)]. The transition dipole moments μ_{XUV} and μ_{FWM} represent allowed transitions between ground states and core-excitonic states [blue and purple arrows in Fig. 2(b)], while the μ_{NIR} represents transitions between the XUV-allowed core-excitonic states and the nearby dark states [red and orange arrows in Fig. 2(b)]. Importantly, the μ_{NIR} dependence of the nonlinear signals probed here distinguishes the selection rules from those of the linear absorption spectrum, which lends the nonlinear techniques greater sensitivity to states within an inhomogeneous linear absorption spectrum. For this reason, there is no guarantee that the entire set of states measured in the linear absorption spectrum will be reproduced in the nonlinear signal emission, especially when the transition dipole moments connect states of such dramatically different relative energies (i.e., μ_{XUV} compared with μ_{NIR}). The peaks appearing at different XUV emission energies in the dark state scans after temporal overlap (with the strongest signal at $\tau_2 = 7$ fs) show that the evolution of some of the dark states coherently excited by the two photon $\mu_{\text{XUV}} + \mu_{\text{NIR1}}$ interaction results in the μ_{NIR2} dipole moments connecting a different set of core-excitons than in the bright state scan. The similarities and differences between the dark state spectrum and the fitted residuals in Fig. 6 support this interpretation.

It is important to note that the very measurement of the bright and dark state time-resolved spectra demonstrates that the bright core-excitonic states and the dark states maintain a coherent relationship for at least 10–20 fs. The double-quantum coherence pathways probed in this technique allow the direct measurement of coherence (dephasing) timescales (known as T_2), which are related to population lifetime (T_1) and environmentally induced pure dephasing (T_2^*) of excited states in the well-known relationship $T_2 = 2T_1 + T_2^*$. In

contrast to gas-phase systems where negligible environmental pure dephasing has been assumed, various sources of pure dephasing can influence the spectral features and temporal dynamics in condensed phase systems as discussed in the following paragraphs.

The comparison between the FWM time zero spectrum and the core-excitons measured over 33.4–33.8 eV in the bright and dark state scans indicates that four distinct core-excitons are all accessible upon initial excitation in this energy range. That is, since the signal pathways accessed in the bright and the dark state scans are equally likely at temporal overlap, the FWM signal emissions from these core-excitonic states cannot be distinguished until the bright and dark state scans are used to independently distinguish these contributions. By contrast, the lower energy range dynamics (33.0–33.4 eV) show that the core-exciton and the coupled dark states require temporal evolution of the excited wave packet to acquire sufficient oscillator strength. The complex spectral dynamics in this range prove the existence of at least one more distinct core-exciton, though more than one state could be implicated from the lack of agreement to the spectral fitting in this range. This lack of agreement on the low energy end of the FWM spectral fit in Fig. 6 is not surprising. These excitonic states, presumed to be at the Γ minimum in earlier studies, clearly shift and perhaps undergo energetic splitting as in the dark state scan on few-femtosecond timescales. The complexity of the observed dynamics, especially at lower emission energies, is underscored by the blueshifting feature in the bright state scans apparently converging to the same emission energy as observed from the dark state scan feature at $\tau_2 = 7$ fs. Collectively, at least five core-excitons have been identified at the Na^+ $L_{2,3}$ edge of NaCl through the attosecond FWM spectra reported here.

B. Physical insight into measured coherence decays: short-range electronic interactions

As shown above, higher-order nonlinear spectroscopies have an advantage over linear spectroscopies for deconvolving inhomogeneously broadened distributions [34]. It is important to contextualize these results with respect to previous literature discussing physical mechanisms for spectral splitting and broadening. The section discusses the origin and processes resulting in the observed spectral inhomogeneity in NaCl. Interestingly, the conclusions drawn from the FWM results above are further corroborated through the comparison between the linear absorption spectrum measured here and further details about the linear spectra elucidated in the literature. The Na^+ $L_{2,3}$ absorption spectrum of the core-exciton in Fig. 1 (inset) shows a doublet splitting of 0.255 eV using the centroid of the broader, higher energy feature (∼33.52 eV), which is in exact agreement with the work of Nakai *et al.* [18]. The peak intensity ratio of 0.26 from Fig. 1 compares very well with the 0.21 ratio reported by Nakai *et al.* [18] for liquid nitrogen temperature spectra; the slightly lower ratio might be expected due to the narrowed line width and greater peak intensity of their 33.55 eV excitonic peak at low temperatures. As mentioned in the Results section, the partial splitting we observe for the two core-exciton states at 33.42 and 33.61 eV underlying the most intense absorption is not discussed in previous XUV literature, but they have been shown in the UV literature possibly due to electron-hole exchange correlation effects observed through lattice strain as measured by piezoreflectivity measurements [29] and changes in crystalline structure in similar alkali chlorides measured by UV absorption [22]. We observed the resolution of these features to diminish after constant irradiation on the same sample volume for extended periods due to the 33.42 eV peak reducing in amplitude. This suggests that the 33.42 eV core-exciton state could be very sensitive to lattice imperfections [22] and crystalline orientation [29] as characterized in the UV for the valence excitons or surface states, as suggested in XUV photoelectron measurements [35]. We note that contributions from surface states are expected to be much less prominent than bulk effects since the measurements reported here are transmission based. Recent calculations of the Na^+ $L_{2,3}$ absorption of many sodium halides suggest that the core-exciton is sensitive to the crystal structure despite its high localization on the Na atom, requiring more detailed theoretical investigations of electronic structure and excitonic interaction on a peak-by-peak basis [37]. Thicker samples also diminished the resolution of the two larger peaks by substantially attenuating the main absorption feature. The difficulty of making and characterizing such thin films does not allow us to confirm single crystallinity of the studied samples (see Appendix B). As a result, we cannot claim that the FWM results and the analysis above apply exclusively to a single crystalline NaCl structure. However, these FWM results definitely reveal more features than the three discernible peaks in the linear absorption spectrum shown in Fig. 1 (inset) through the spectral deconvolution. While the doublet spectral shape of the linear absorption, consisting of the splitting between the peak at 33.27 eV and the two overlapped features making up the main peak with its centroid at 33.52 eV, is generally described through the lens of spin-orbit coupling, the following discussion points out that a refined description of the core-exciton line shapes and amplitudes is still debated, and the alkali halide core-excitonic properties are not completely understood.

Spectra at liquid nitrogen temperature reported by Nakai *et al.* [18] show that the core-exciton peaks are much broader than the valence-exciton peaks and that the core-exciton line shapes cannot be described simply by electron-phonon broadening. More precisely, the Na^+ core-excitonic absorptions in NaCl are not adequately represented by a large progression of phonon states underlying the peaks. While the large effective mass of the Na $2p$ core-hole should enhance exciton-phonon coupling, the strong coupling regime is expected only when sufficient energy in the absorption bandwidth is available to excite many phonons (e.g., >10 phonons) [38]. The NaCl acoustic phonon spectrum spans 9–23 meV, and the longitudinal-optical phonons are in the range of 24–40 meV [39–41]. The Gaussian line shapes observed here for Na^+ core-excitonic states (e.g., the spectral fits in Fig. 6) suggest that exciton-phonon coupling is not within the strong regime for the Na^+ core-excitonic states, as the peaks measured by FWM are too narrow to allow for a significant population of phonons—especially the longitudinal-optical phonons that typically drive exciton-phonon couplings. Interestingly, the results here suggest that exciton-phonon coupling in NaCl does not exert as much influence over the core-exciton as

has been recently discussed for another ionic insulator MgO, where exciton-phonon coupling decreases the core-exciton decay times considerably [33]. Thus, the rapid dephasing dynamics measured for NaCl are expected to originate from electronic perturbations, as discussed below.

Auger decay processes for the Na^+ core-exciton in NaCl, in which the core-excitonic state decays by the $2p$ core-hole being filled by another electron that destroys the Coulombically bound relationship between Na^+ $3s$ electron and the $2p$ core-hole, are not currently known well enough to fully account for the measured line broadening either. Photoemission studies report average Auger lifetimes for the Na $2p$ core-hole in NaCl of 30 meV (138 fs) with rather large uncertainty, permitting lifetimes up to 60 meV (69 fs) [42]. Nakai *et al.* [18] cite a 10 meV (414 fs) Auger decay and invoke electron-electron interactions between core-excitons and a continuous band of nearby states to describe the low-temperature core-exciton spectra. Since the broad, quasicontinuous band of valence-level states that embeds the Na^+ core-exciton reflect the ionic sharing of the Na $3s$ electron with the Cl $3p$ orbital, the electron-electron interactions between the Na $3s$ electron shared with the Cl and the Na^+ $3s$ electron of the core-exciton may contribute to the observed coherent dephasing dynamics. While the 66 and 98 meV bandwidths extracted for the core-excitonic states resolved at 33.42 and 33.61 eV are equivalent to 62 and 42 fs lifetimes, respectively, the time-domain FWM measurements here show faster coherence decays than expected from the currently reported Auger lifetime broadening. This is suggestive of more complex dephasing mechanisms at play for these core-excitonic states which will require in-depth theoretical investigations to determine fully.

The relative intensities of the doublet peaks are widely known to deviate from the 2:1 ratio expected by considering state multiplicity [19,21–24,26]. Onodera and Toyozawa [24] introduce exchange interaction between the electron and hole, which results in increased mixing of the excited electron and core-hole states, to account for the different doublet peak intensity ratios. Using their model to analyze the linear absorption spectra, the electron-hole exchange interaction and spin-orbit interaction are extracted, respectively, as 0.0438 and 0.1149 eV for the valence excitons and 0.24 and 0.21 eV for the Na^+ core-excitons [18,24,25]. Applying the Onodera-Toyozawa model to the centroids of the general doublet structure in the 33.0–33.8 eV range of Fig. 1, our linear absorption agrees well with the previously reported exchange interaction and spin-orbit splitting for the Na^+ core-excitons [18,19,29]. This fact, alongside the proof from the FWM data (Figs. 5 and 6) that several core-excitons underlie this general doublet structure of the linear absorption spectrum, strengthens support for the existence of at least five distinct core-excitons at the Na^+ $L_{2,3}$ edge. With the exciton exchange interaction influencing the physical behaviors of at least five Na^+ core-excitons identified to underly the Na $L_{2,3}$ absorption edge, the rapid dephasing times measured in the FWM experiments could be understood to result from mixing between core-excitons, providing multiple short-range electronic perturbations to and increased relaxation channels for these core-excitonic states. Finally, greater peak multiplicities than the doublet for the alkali halide excitons have also been measured by reflectivity [26,29], transmission [22], low energy electron loss [28], and photoelectron spectroscopy [35] and predicted [27,30,37] to arise from the crystal field symmetry surrounding the alkali atom and varied crystalline orientations. Collectively, the above alkali halide exciton literature suggests that the prominent doublet structure may, in fact, be composed of an inhomogeneous distribution of core-excitons with a complex array of physical processes governing their properties. The FWM data reported here offer further evidence toward this end.

IV. CONCLUSIONS

These experimental insights divulge a wealth of information about the distributions of core-excitons in the prototypical ionic insulator NaCl, studied here in polycrystalline 50-nm-thick films. The localized nature of the electron and hole to the Na^+ ion suggests that the identified core-excitons with inhomogeneous line shapes result from additional short-range perturbations. A combination of strong electron-hole exchange interactions and electron-electron correlations yield spectral features with weak perturbations due to the likely polycrystalline structure, augmented by broadening due to the phonon spectrum and site imperfections. An in-depth theoretical treatment is needed to visualize and more accurately describe the nature and dynamics of the core-excitons observed in the bright and dark state scans at the Na^+ $L_{2,3}$ edge. A complete picture of the physical mechanisms responsible for these features requires further theoretical developments to accurately and simultaneously treat spin-orbit coupling, electron-hole exchange correlation, and multielectron correlations.

Strong connections between well-studied phenomena in atomic physics and the exciton literature from the solid state physics community have been established with this study. The implementation of nonlinear wave mixing spectroscopy with XUV and NIR pulses described here is uniquely able to measure the effect of dark states on core-excitonic properties; time-dependent splitting of core-excitonic states is observed, resulting from the evolution of XUV-dark states. We have shown direct evidence that the Na^+ core-exciton doublet spectrum is composed of several inhomogeneously broadened excitons with < 10 fs coherence lifetimes. Our technique complements time-resolved transient-grating spectroscopies using XUV pulses generated at XFELs by exploiting resonant, phase-matched transitions between atomic-like states in a solid state system to directly measure few-femtosecond dynamics in the time domain. The tabletop experiments discussed here directly access ultrafast, highly localized, atom-like electronic properties that are expected to occur at single-nanometer length scales and smaller. A bridge between the attosecond atomic and molecular optics researchers and the solid state physics community has been built, expanding the possibilities of future explorations in condensed matter and materials science that require atomic specificity and sub-femtosecond temporal resolution.

ACKNOWLEDGMENTS

The authors thank Romain Géneaux for fruitful discussions of the data and interpretation. This work was performed by

personnel and equipment supported by the Office of Science, Office of Basic Energy Sciences through the Atomic, Molecular and Optical Sciences Program of the Division of Chemical Sciences, Geosciences, and Biosciences of the U.S. Department of Energy at LBNL under Contract No. DE-AC02-05CH11231. Motivation for this work was provided by recently supported research through Air Force Office of Scientific Research (AFOSR), Grant No. FA9550-20-1-0334. J.D.G. is grateful to the Arnold and Mabel Beckman Foundation for support as an Arnold O. Beckman Postdoctoral Fellow. A.P.F. acknowledges support from the National Science Foundation Graduate Research Fellowship Program. Y-C.L. acknowledges financial support from the Taiwan Ministry of Education. H.-T.C., M.Z., and S.R.L. acknowledge support from the AFOSR (FA9550-15-1-0037 and FA9550-19-1-0314) and the W.M. Keck Foundation (No. 046300). M.Z. acknowledges funding from the W.M. Keck Foundation (No. 993922), the U.C. Office of the President within the Multicampus Research Programs and Initiatives (M21PL3263), and the Laboratory Directed Research and Development Program at LBNL (107573).

J.D.G., A.P.F., Y-C.L., D.M.N., and S.R.L. designed the experiments; H.-T.C. and M.Z. observed the first ATA core-excitonic signals in NaCl, which formed the basis for the FWM experimental campaign; S.R.L. proposed the FWM experiments based on the previous observations of H.-T.C. and M.Z. using ATA spectroscopy. J.D.G., A.P.F., and Y-C.L. performed the FWM experiments; J.D.G. conducted the analysis; J.D.G., A.P.F., Y-C.L., H.-T.C., M.Z., D.M.N., and S.R.L. discussed results; J.D.G. wrote the paper.

APPENDIX A: METHODS—ATTOSECOND FWM APPARATUS

The output of a Ti:sapphire laser (Femtopower, 1 kHz repetition rate, 1.7 mJ/pulse, 22 fs, 780 nm) is spectrally broadened in a 2-m-long stretched hollow core fiber of 500 μm inner diameter (Few-Cycle Inc.) filled with 2.1 bar of neon gas. Seven pairs of double angled chirped mirrors (Ultrafast Innovations, PC70), fused silica wedge pairs, and 2 mm of ammonium dihydrogen phosphate (ADP) crystal are used to temporally compress the pulses to <6 fs durations, providing compressed broadband NIR pulses spanning 550–950 nm with ~600 μJ/pulse energies. The beam is then split by a 75:25 (R:T) beam splitter to separate the pulse used to create the XUV pulse ($\mathbf{k}_{\mathrm{XUV}}$) from the pulse used to generate the two noncollinear NIR beams ($\mathbf{k}_{\mathrm{NIR1}}$ and $\mathbf{k}_{\mathrm{NIR2}}$). The reflected beam is focused by a concave silver mirror ($f = 50$ cm) into a vacuum apparatus at 10^{-6} Torr containing a gas flow cell with krypton at ~4 Torr for HHG. The interaction of the few-cycle NIR field with the krypton gas generates an attosecond pulse train of 2–3 subfemtosecond XUV bursts in the 25–45 eV range. A vertically adjustable Al foil (0.15 μm thickness, Lebow) attenuates the copropagating NIR field used to drive the HHG process to spectrally isolate the XUV pulse. The transmitted XUV pulse is refocused by a gold-coated toroidal mirror through the annular mirror into a NaCl thin film sample. The XUV intensity at the sample is estimated to be ~10^{10} W cm^{-2} on the sample due to the low HHG efficiency.

The transmitted pulse of the 75:25 beam splitter is delayed relative to the XUV beam using a piezoelectric translation stage (P-622 with E509 controller, Physik Instrumente) for control over τ_1, and then the beam is split with a 50:50 beam splitter to form NIR_1 (reflection) and NIR_2 (transmission). Control over τ_2 is achieved by routing NIR_2 onto a second piezoelectric translation stage. Two concave silver mirrors ($f = 1$ m) then direct NIR_1 and NIR_2 above and below the annular mirror aperture, respectively, and spatially overlap them with the XUV beam on the sample. A finely adjustable iris is placed before the 50:50 beam splitter to systematically attenuate the noncollinear NIR beams. The NIR_1 (NIR_2) beam diameters at focus are characterized using a beam profiler (DataRay WinCamD) to be 300 μm (350 μm) at FWHM intensity for this work. A slight ellipticity of NIR_2 explains the relative trend in fluences shown in Fig. 4. Temporal and spatial overlap is determined by ATA signal of Ar gas (14.5 Torr) provided by a 1 mm gas cell accessible with a motorized sample translation stage. The NIR pulse envelope is estimated at 5.6 fs from the rise time of the Ar $3s4p$ autoionization signal measured by ATA (see Supplemental Material, Fig. SM3 [36]). A vertically adjustable Al foil (0.15 μm, Lebow) attenuates the noncollinear NIR beams after the sample. The transmitted XUV light is spectrally dispersed in the horizontal plane by a gold-coated flat-field grating (01-0639, Hitachi) and recorded using a 1340 × 400-pixel x-ray CCD camera (Pixis XO 400-B, Princeton Instruments). The wave mixing signals can be isolated and optimized using the two vertically adjustable filters, an automated iris placed right after the toroidal mirror, and a vertically translatable camera mount that allows for the unwanted ATA signals to be translated off the CCD imaging area. Typically, the HHG alignment is optimized for photon flux and narrowest vertical intensity distribution for the XUV beam imaged on the CCD. Very fine adjustments of the filters and the iris are then used to spatially filter the vertical intensity profile of $\mathbf{k}_{\mathrm{XUV}}$ such that FWM signals at small $\theta_{\mathrm{emission}}$ can be well separated from overlap with ATA signals and residual scatter from $\mathbf{k}_{\mathrm{XUV}}$; this is increasingly necessary at higher XUV energies due to phase-matching angles. The bright and dark state scans were acquired with 10 000 laser pulses for each time step and scanned with 1 fs steps. Each spectrum in the fluence dependent studies was acquired with 14 000 laser pulses at temporal overlap.

APPENDIX B: NaCl THIN FILM SAMPLES

The samples are NaCl microcrystalline thin films (Lebow) deposited on 30-nm-thick Si_3N_4 membranes (Norcada NX5050X). NaCl thin films of 50 nm thickness were used in the studies reported here. A range of thin film thicknesses including 30, 50, and 70 nm, as well as a 120 nm film on a 50 nm substrate were initially tested to optimize experimental signal while avoiding propagation effects and signal reabsorption. The properties and purity of submicron thin films are difficult to measure—especially at <100 nm thicknesses. Lebow indicates the evaporant used during NaCl deposition is 99.9% pure and that such thin films are typically microcrystalline; therefore, it is very unlikely the films are single crystalline. A NaCl film thickness of 50 nm was found

to provide a good compromise between signal strength and self-absorption. Dramatic spectral changes in films >100 nm have been reported such as strong attenuation of absorption features [18,19]. The samples are mounted on a three-axis translation stage at the focal point of all three beams. The illuminated area was refreshed every minute using vertical and horizontal sample translation to avoid artifacts from sample heating and damage. The gas flow cell used for external calibrations and finding spatial and temporal overlap is dually mounted on the translation stage. Samples were received under N_2 purge and stored in a vacuum chamber to avoid sample contamination.

[1] P. M. Kraus, M. Zürch, S. K. Cushing, D. M. Neumark, and S. R. Leone, The ultrafast x-ray spectroscopic revolution in chemical dynamics, Nat. Rev. Chem. **2**, 82 (2018).

[2] L. Young *et al.*, Roadmap of ultrafast x-ray atomic and molecular physics, J. Phys. B **51**, 032003 (2018).

[3] K. Bennett, Y. Zhang, M. Kowalewski, W. J. Hua, and S. Mukamel, Multidimensional resonant nonlinear spectroscopy with coherent broadband x-ray pulses, Phys. Scripta **2016**, 014002 (2016).

[4] A. Picon, J. Mompart, and S. H. Southworth, Stimulated Raman adiabatic passage with two-color x-ray pulses, New J. Phys. **17**, 083038 (2015).

[5] S. Mukamel, D. Healion, Y. Zhang, and J. D. Biggs, Multidimensional attosecond resonant x-ray spectroscopy of molecules: lessons from the optical regime, Annu. Rev. Phys. Chem. **64**, 101 (2013).

[6] R. K. Lam *et al.*, Soft X-ray Second Harmonic Generation as an Interfacial Probe, Phys. Rev. Lett. **120**, 023901 (2018).

[7] S. Tanaka and S. Mukamel, X-ray four-wave mixing in molecules, J. Chem. Phys. **116**, 1877 (2002).

[8] A. P. Fidler, H. J. B. Marroux, E. R. Warrick, E. Bloch, W. Cao, S. R. Leone, and D. M. Neumark, Autoionization dynamics of $(^2P_{1/2})ns/d$ states in krypton probed by noncollinear wave mixing with attosecond extreme ultraviolet and few-cycle near infrared pulses, J. Chem. Phys. **151**, 114305 (2019).

[9] E. R. Warrick, A. P. Fidler, W. Cao, E. Bloch, D. M. Neumark, and S. R. Leone, Multiple pulse coherent dynamics and wave packet control of the N_2 $a''\,{}^1\Sigma_g^+$ dark state by attosecond four-wave mixing, Faraday Discuss. **212**, 157 (2018).

[10] F. Bencivenga, R. Cucini, F. Capotondi, A. Battistoni, R. Mincigrucci, E. Giangrisostomi, A. Gessini, M. Manfredda, I. P. Nikolov, E. Pedersoli, E. Principi, C. Svetina, P. Parisse, F. Casolari, M. B. Danailov, M. Kiskinova, and C. Masciovecchio, Four-wave mixing experiments with extreme ultraviolet transient gratings, Nature **520**, 205 (2015).

[11] R. Bohinc *et al.*, Nonlinear XUV-optical transient grating spectroscopy at the Si $L_{2,3}$ edge, Appl. Phys. Lett. **114**, 181101 (2019).

[12] L. Foglia, F. Capotondi, R. Mincigrucci, D. Naumenko, E. Pedersoli, A. Simoncig, G. Kurdi, A. Calvi, M. Manfredda, L. Raimondi, N. Mahne, M. Zangrando, C. Masciovecchio, and F. Bencivenga, First Evidence of Purely Extreme-Ultraviolet Four-Wave Mixing, Phys. Rev. Lett. **120**, 263901 (2018).

[13] F. Bencivenga *et al.*, Nanoscale transient gratings excited and probed by extreme ultraviolet femtosecond pulses, Sci. Adv. **5**, eaaw5805 (2019).

[14] W. Cao, E. R. Warrick, A. Fidler, D. M. Neumark, and S. R. Leone, Noncollinear wave mixing of attosecond XUV and few-cycle optical laser pulses in gas-phase atoms: toward multidimensional spectroscopy involving XUV excitations, Phys. Rev. A **94**, 053846 (2016).

[15] W. Cao, E. R. Warrick, A. Fidler, S. R. Leone, and D. M. Neumark, Excited-state vibronic wave-packet dynamics in H_2 probed by XUV transient four-wave mixing, Phys. Rev. A **97**, 023401 (2018).

[16] J. Kim, S. Mukamel, and G. D. Scholes, Two-dimensional electronic double-quantum coherence spectroscopy, Acc. Chem. Res. **42**, 1375 (2009).

[17] R. Grasser and A. Scharmann, in *Collective Excitations in Solids*, edited by B. Di Bartolo (Springer US, Boston, 1983), p. 317.

[18] S. I. Nakai, T. Ishii, and T. Sagawa, Core exciton absorption in sodium halides, J. Phys. Soc. Jpn. **30**, 428 (1971).

[19] S. I. Nakai and T. Sagawa, Na^+ $L_{2,3}$ absorption spectra of sodium halides, J. Phys. Soc. Jpn. **26**, 1427 (1969).

[20] M. Iwan and C. Kunz, Photoemission investigation of autoionizing Na^+ $2p$ core excitons in NaCl, J. Phys. C Solid State **11**, 905 (1978).

[21] R. Haensel, G. Keitel, G. Peters, P. Schreiber, B. Sonntag, and C. Kunz, Photoemission Measurement on NaCl in Photon Energy Range 32–50 eV, Phys. Rev. Lett. **23**, 530 (1969).

[22] J. E. Eby, K. J. Teegarden, and D. B. Dutton, Ultraviolet absorption of alkali halides, Phys. Rev. **116**, 1099 (1959).

[23] R. S. Knox and N. Inchauspe, Exciton states in ionic crystals, Phys. Rev. **116**, 1093 (1959).

[24] Y. Onodera and Y. Toyozawa, Excitons in alkali halides, J. Phys. Soc. Jpn. **22**, 833 (1967).

[25] T. Miyata and T. Tomiki, Optical studies of NaCl single crystals in 10 eV region II. The spectra of conductivity at low temperatures, absorption constant and energy loss, J. Phys. Soc. Jpn. **24**, 1286 (1968).

[26] P. L. Hartman, J. R. Nelson, and J. G. Siegfried, Reflection spectrum and structure in the exciton absorption peak of NaCl and KCl, Phys. Rev. **105**, 123 (1957).

[27] T. Aberg and J. L. Dehmer, Role of highly localized excitons in photoabsorption spectra of ionic-crystals, J. Phys. C Solid State **6**, 1450 (1973).

[28] T. Mabuchi, H. Toda, and H. Yamanaka, Core exciton of alkali and alkali-earth halides, J. Phys. Soc. Jpn. **62**, 246 (1993).

[29] M. Yuri, S. Sato, Y. Seto, H. Hayashi, and H. Fukutani, Electron-hole exchange interaction of the Γ-exciton in NaCl studied by piezoreflectivity, J. Phys. Soc. Jpn. **62**, 818 (1993).

[30] A. W. Overhauser, Multiplet structure of excitons in ionic crystals, Phys. Rev. **101**, 1702 (1956).

[31] C. E. Moore, *Atomic Energy Levels* (National Bureau of Standards, Washington, D.C., USA, 1971), Vol. I, pp. 91–92.

[32] A. Moulet, J. B. Bertrand, T. Klostermann, A. Guggenmos, N. Karpowicz, and E. Goulielmakis, Soft x-ray excitonics, Science **357**, 1134 (2017).

[33] R. Géneaux, C. J. Kaplan, L. Yue, A. D. Ross, J. E. Bækhøj, P. M. Kraus, H.-T. Chang, A. Guggenmos, M.-Y. Huang,

M. Zürch, K. J. Schafer, D. M. Neumark, M. B. Gaarde, and S. R. Leone, Attosecond Time-Domain Measurement of Core-Level-Exciton Decay in Magnesium Oxide, Phys. Rev. Lett. **124**, 207401 (2020).

[34] S. Mukamel, *Principles of Nonlinear Optical Spectroscopy* (Oxford University Press, New York, 1995).

[35] M. Kamada, O. Aita, K. Ichikawa, and K. Tsutsumi, Decay of the Na $2p$ core exciton in sodium-halides studied by photoelectron-spectroscopy, Phys. Rev. B **36**, 4962 (1987).

[36] See Supplemental Material at http://link.aps.org/supplemental/10.1103/PhysRevB.103.245140 for Figs. SM1–SM3 and Tables SM1–SM2.

[37] K. Tomita, T. Miyata, W. Olovsson, and T. Mizoguchi, Core-exciton interaction in sodium $L_{2,3}$ edge structure investigated using the Bethe-Salpeter equation, J. Phys. Chem. C **120**, 9036 (2016).

[38] P. H. Citrin, P. Eisenber, and D. R. Hamann, Phonon Broadening of X-Ray Photoemission Linewidths, Phys. Rev. Lett. **33**, 965 (1974).

[39] G. Raunio and S. Rolandson, Lattice dynamics of NaCl, KCl, RbCl, and RbF, Phys. Rev. B **2**, 2098 (1970).

[40] E. R. Cowley, S. Satija, and R. Youngblood, Line-shapes of longitudinal-optic phonons in sodium-chloride at 300 K and 600 K, Phys. Rev. B **28**, 993 (1983).

[41] G. D. Mahan, Photoemission from alkali-halides—energies and line-shapes, Phys. Rev. B **21**, 4791 (1980).

[42] G. K. Wertheim, J. E. Rowe, D. N. E. Buchanan, and P. H. Citrin, Experimental interatomic Auger rates in sodium-halides, Phys. Rev. B **51**, 13669 (1995).